IEEE Access
Multidisciplinary | Rapid Review | Open Access Journal

Received March 6, 2020, accepted March 14, 2020, date of publication March 18, 2020, date of current version March 27, 2020.

Digital Object Identifier 10.1109/ACCESS.2020.2981720

Multi-Resolution Intrinsic Texture Geometry-Based Local Binary Pattern for Texture Classification

NUH ALPASLAN AND KAZIM HANBAY
Computer Engineering Department, Bingöl University, 12000 Bingöl, Turkey
Corresponding author: Nuh Alpaslan (nalpaslan@bingol.edu.tr)

ABSTRACT In this paper, we propose a new hybrid Local Binary Pattern (LBP) based on Hessian matrix and Attractive Center-Symmetric LBP (ACS-LBP), called Hess-ACS-LBP. The Hessian matrix provides the directional derivative information of different texture regions, while ACS-LBP reveals the local texture features efficiently. To obtain the macro- and micro-structure textural changes, Hessian matrix is calculated in a multiscale schema. Multiscale Hessian matrix presents the intrinsic local geometry of the texture changes. The magnitude information of the Hessian matrix is used in the ACS-LBP method. A cross-scale joint coding strategy is used to construct Hess-ACS-LBP descriptor. Finally, histogram concatenation is carried out. Extensive experiments on eight texture databases of CUReT, USPTex, KTH-TIPS2b, MondialMarmi, OuTeX TC_00013, XU HR, ALOT and STex validate the efficiency of the proposed method. The proposed *Hess-ACS-LBP* method achieves about 20% improvement over the original LBP method and 1%–11% improvement over the other state-of-the-art hand-crafted LBP methods in terms of classification accuracy. Besides, the experimental results show that the proposed method achieves up to 32% better results than the state-of-the-art deep learning based methods. Especially, the performance of the proposed method on ALOT and STex datasets containing many classes is remarkable.

INDEX TERMS Hessian matrix, feature extraction, local binary patterns, texture classification.

I. INTRODUCTION

Texture analysis is one of the basic operations which is used in the fields of image processing, pattern recognition, and computer vision. The texture is one of the most important characteristics to detect objects in the region of interest in the image. It is aimed to obtain the distinctive features of different classes in images by texture analysis. Different textures in the images can be classified by obtaining unique features that define each class. However, rotation, illumination, and perspective changes, especially in the same class in images, are the most fundamental problems that make texture analysis and classification difficult [1]. Therefore, analyzing images using only features such as color and edge information does not give the desired results. As a result, effective results have been obtained using feature extraction methods that analyze images with different and powerful approaches. The main property of these methods is that they can effectively apply local texture representations throughout the image.

Texture classification generally includes two significant subproblems: texture representation and classification [1]. Texture representation, that is the extraction of the base features that define the texture, is the basis building block of texture analysis. The extraction of strong and distinctive textural primitives has an important effect. If texture representation is not performed effectively by feature extraction, the desired results will not be obtained even if the best classifier is used. For this reason, the texture classification problem continues to be an area of intense interest due to the use of different imagers and constantly developing imaging technologies. The need for the development and use of effective texture analysis and representation methods continues, especially in applications such as medical image analysis, content-based image retrieval, aerial imagery analysis, biometrics and face recognition. An excellent review of the texture analysis and representation paradigm can be found in [1]. As a result, a representative texture representation and modeling method are developed in this paper.

In this study, the 2-D Hessian matrix-based LBP method (Hess-ACS-LBP) was developed in order to better characterize the intra-class and inter-class variation in texture images.

The associate editor coordinating the review of this manuscript and approving it for publication was Wenming Cao.

The Hessian matrix was calculated using Gaussian derivative filters in Hess-ACS- LBP method. The sigma σ parameter used in the design of Gaussian derivative filters was evaluated using different values. Thus, for each σ value derivative filters were designed and the Hessian matrix was calculated using these filters. Consequently, by calculating different Hessian matrices for different σ values, second-order differential features of texture images in multiple scales were obtained. The Hessian matrix was calculated for each σ value and the 2-D joint histogram was computed using the LBP of the gray level image. The 2-D joint histogram with different resolutions was concatenated to obtain the final feature vector. The main contributions of the proposed method are highlighted as follows:

- The intra-class and inter-class variation of texture patterns with local and regional pixel variations were determined by using the Hessian matrix.
- Differential texture characterization was performed with the multi-resolution Hessian matrix, which works as a curvature tensor, containing information on all directions. The obtained differential features were combined with the Hess-ACS-LBP method and textures were effectively classified.
- As an alternative to similar hybrid LBP methods, a novel LBP method has been developed with higher classification performance and lower computational complexity.

The outline of the study is given below. Section II summaries previous texture representation and analysis literature. A brief review of the related methodology used in this paper, including the Hessian matrix and LBP, is given in Section III. Section IV describes the proposed texture classification method. In Section V, the experimental results are performed on different datasets and the results of the proposed method are compared with the literature. In Section VI, we present a discussion on the classification results. Conclusions and future work are summarized in Section VII.

II. PREVIOUS WORKS

The basic characteristics of texture structures in the image must encode and analyze to perform effective image analysis. In the literature, there are many texture feature extraction methods [2]. These methods are generally divided into four categories: statistical methods [3]–[5], model-based methods [6], [7], structural methods [8], [9] and filter-based methods [3], [10]. Statistical and model-based methods often analyze spatial relations of pixels based on small pixel neighborhoods. The best known of these methods are gray level co-occurrence matrices (GLCM) [11], Markov random field model (MRF) [12] and local binary patterns (LBP) [13], [14]. Structural methods characterize the texture based on regular layouts of textural primitives [8]. The classification of images with regular texture patterns, with structural texture analysis methods using morphological operators, gives effective results [9], [15]. Many texture analysis and classification methods have been developed by using filter-based methods such as Wavelet transform [16], Gabor transform [17], [18] and filter banks [3], [10]. Multiple subbands of images are obtained by using different main wavelet functions in wavelet transform-based methods. Different textural information can be obtained through multiple resolution analysis. Subband images are modeled with General Gaussian Model (GGM) or Gaussian Mixture Model (GMM). Thus, parameters with reduced size and distinctiveness are obtained. However, the high computational cost and the low classification performance in noise conditions are the major weaknesses of the wavelet transform method. Gabor filters are linear filters used in signal analysis. Gabor filters with different scales and angles designed similarly to the human vision system can perform rotation invariant texture analysis [17]. In another recent study in [19], image classification was performed using texture features obtained from Gaussian derivative filters. Gaussian (DOG) filters and the difference of offset Gaussian (DOOG) filters were constructed and filter responses were obtained by convolution. Both the filter responses corresponding to the image region and the responses of different texture boundaries were obtained with these filters. The distinctive and unique features were calculated thanks to this data. Apart from these methods, very successful texture classification studies have been carried out with methods such as histogram-oriented gradients (HOG) and co-occurrence histogram-oriented gradients (CoHOG) [20], [21] and local directional number pattern (LDN) [22].

As it is known, texture classification algorithms consist of two main steps. The first step is to extract the characteristic textural features. In the second step, the classification process is carried out by using the obtained features to distinguish the different texture types. In recent years, feature extraction and classification procedures have been performed together using convolutional neural networks (CNNs) approaches. A typical CNN architecture usually consists of connecting multiple convolution layers, followed by the fully connected layers and the SoftMax classifier. Unlike hand-crafted features, fully connected layer features learned from CNN contain high-level semantic information [23]. Therefore, effective texture classification studies have been performed using CNN architectures [24], [25]. Qi *et al.* [24] developed the CNN architecture as a feature extractor to classify dynamic texture and scene images. They calculated the first and second-order statistics on the deep characteristics of each image. By applying the proposed Transferred ConvNet Feature (TCoF) scheme in two different ways, the features of consecutive video frames are calculated and it is given as an input to the classifier. Talo *et al.* have been classified as normal and abnormal Magnetic resonance (MR) images by deep transfer learning methods [26]. ResNet34 was used as a deep learning model. The boundaries and position of the object at different positions were calculated using region-based convolutional neural networks (R-CNNs) for real-time object detection [27]. When deep learning-based studies are examined, it is seen that there are some superior and weak points. Firstly, high accuracy and detailed descriptive information are the most important advantages. However, the high computational cost, the need for high dimensional data for the learning process, and the hardware requirement

seem to be the most important weaknesses. Therefore, the need for conventional feature extraction methods still continues. Therefore, studies on the development of traditional and powerful methods such as Local Binary Pattern, wavelet transform, curvelet transform and Gabor transform are ongoing [28].

The LBP, which is developed by Ojala *et al.*, is an effective gray-level texture operator that calculates the spatial characteristics of gray-level images [13], [14]. Many LBP based methods have been proposed to improve the performance of this method [29]. Thus, LBP methods with low computational complexity and high discrimination power have been developed. The developed methods make the LBP method invariant to noise, rotation changes [30]. As a result, it is used extensively in areas such as texture classification [31], smoke detection [32], facial expression recognition [33]–[35] and medical image processing [36].

The center-symmetric LBP (CS-LBP) method developed by Heikkila *et al.* compares the central symmetric pairs of pixels instead of comparing the central pixel with its neighbors [37]. The dominant LBP (DLBP) method was developed by selecting dominant patterns from all the patterns in the image experimentally [38]. The DLBP method is more resistant to rotation, noise, and histogram equalization situations than the LBP method. In the Weber Local Binary Pattern (WLBP) method, combines the advantages of Weber Local Descriptor and LBP [39]. The differential excitation and the LBP code of input image were obtained according to both methods. The WLBP histogram was constructed using these two images. Kaya *et al.* proposed two different LBP descriptors [40]. The first method is based on modeling the relationship between 8 adjacent pixels. The comparisons are made not only between the adjacent neighboring pixels but also with the neighbors defined by the distance parameter. In the second method, a different approach is used to determine micro-patterns. Assuming that some texture patterns may not be observed in circular searches, pixel relationships were analyzed according to different angle values. The local binary pattern for color images (LBPC) method utilizes a plane to threshold color pixels in the neighborhood of a local window into two categories [41]. To increase the distinctive ability of the method, the LBP of the hue component of HSI color space was utilized (LBPH). Lee *et al.* [42] proposed the local color vector binary patterns (LCVBPs) method for the face recognition problem. The LCVBPs method consists of two basic parts, color norm patterns, and color angular patterns. The color angular pattern computes the high distinctive features of the two-color spectrum and derives the spatial correlation of the local color texture. The local concave and convex microstructure patterns (LCvMSP and LCxMSP) have been developed to perform robust texture analysis [43]. Local concave-and-convex features allow all triplets to be defined and divided as concave and convex micro-structures around the central pixel. These features reveal the local fluctuations of texture patterns and express changes. The obtained concave and convex features are thresholded using binary thresholding functions. Thus, the pixels along a closed path around the central pixel are characterized in detail. El Khadiri *et al.* [44] developed two novel LBP methods called repulsive and attractive local binary gradient contours (RLBGC and ALBGC). The RLBGC and ALBGC methods encode differences between local density values around the center pixel of the 3×3 gray-scale image patch. In addition, the robustness of the method has been increased by modeling the relationship between the average local and average global gray levels and the central pixel values. In a recent method in [45], LBP and principal curvatures were used together and a different perspective is given to the LBP literature. The principal curvatures of the gray level image calculated at different scales and rotation invariant uniform LBP $LBP^{riu2}_{P,R}$ were used together. A 2-D joint histogram was constructed using LBP matrices with the principal curvatures calculated on each scale. All the histograms were concentrated to obtain the PCLBP feature. The experimental results show that the use of differential operations with LBP method positively effects the classification performance [45].

III. RELATED WORK

In this section, we present an overview of the Hessian matrix and the LBP-like methods developed for the texture images. Merits and demerits of each method are explained below.

A. HESSIAN MATRIX

In many computer vision and image processing applications, it is important to calculate distinctive and explicit features from the images. The first step is the detection of different points in the image. These can be a corner, edge or an intensity blob of an object in the image. In the next step, the area around the detected point is defined. In the last step, matching is done. In the photographs taken from two different perspectives of the same scene, the information of the same point is matched using similarity criteria in both images. There are different algorithms for performing these steps. From the point of view of the texture classification problem, the focus will be the detection step. The Hessian matrix comes to mind at this point. The Hessian matrix was used by some researchers to detect and analyze the specific shapes [46].

The Hessian matrix acts as a curvature tensor containing information in all directions. However, the direction with the lowest and highest curvature is important. The information is available in the eigenvectors and eigenvalues of the Hessian matrix. In the literature, by analyzing the eigenvector and eigenvalue of the Hessian matrix, local geometrical feature informations of the images were extracted [47]. The Hessian matrix contains geometric information about the image surface. The determinant of the Hessian matrix expresses the positive or negative value of the curvature of the surface. The geometrical labeling and classification of the image surface are carried out with the signs of surface curvatures [48]–[50].

B. TRADITIONAL LOCAL BINARY PATTERN (LBP)

In the original LBP method, the center pixel is determined by comparing it with its neighboring pixels [14]. The LBP code is calculated as in Eq. (1).

$$LBP_{P,R} = \sum_{p=0}^{P-1} s(g_p - g_c)2^p \tag{1}$$

where g_c represents the gray level intensity value of the center pixel and g_p represents the value of the respective neighboring pixel of the center pixel. The P is the number of neighbors and R is the radius of the circular neighborhood. The $s(x)$ is the indicator function, defined as in Eq. (2).

$$s(x) = \begin{cases} 1 & x \geq 0 \\ 0 & x < 0 \end{cases} \tag{2}$$

Different versions of the LBP method have been developed to improve the efficacy in different textural conditions [14]. These are uniform, rotation-invariant, and rotation-invariant uniform LBP methods. The uniform value of an LBP pattern refers to the number of circular spatial transitions and is defined as in Eq. (3).

$$U(LBP_{P,R}) = \left|s(g_{p-1} - g_c) - s(g_0 - g_c)\right| + \sum_{p=1}^{P-1} \left|s(g_p - g_c) - s(g_{p-1} - g_c)\right| \tag{3}$$

In Eq. 3, if $U \leq 2$, LBP patterns are assigned to uniform patterns. In other cases, LBP patterns are classified as non-uniform patterns. To achieve the rotation invariance, the rotation invariant LBP is defined as in Eq. (4).

$$LBP^{riu2}_{P,R} = \begin{cases} \sum_{p=0}^{P-1} s(g_p - g_c) & U(LBP_{P,R}) \leq 2 \\ P+1 & otherwise \end{cases} \tag{4}$$

C. ATTRACTIVE AND REPULSIVE CENTER-SYMMETRIC LOCAL BINARY PATTERNS (ACS-LBP AND RCS-LBP)

There are many LBP methods based on pixel neighborhoods that are considered symmetrically around the central pixel. Although these methods have many advantages, the determination of the appropriate threshold value is an important problem. The threshold value leads to undesirable sensitivities especially in flat image regions and images with shadow. Additionally, local and global textural features in the image can be ignored by bringing the center pixel to the foreground. Besides, the conventional LBP operator has some disadvantages [51]. Although the two center pixels have different gray-scale values, they have the same LBP code as shown in Fig. 1. This situation reduces the discriminative ability of LBP, LTP, and CS-LBP for texture classification. Besides, it makes LBP sensitive to image rotation, to lose local textural information due to its quantization procedure. el Merabet *et al.* [51] proposed two novel LBP methods called ACS-LBP and RCS-LBP to solve these problems. In these methods, the relationship between the center pixel and the

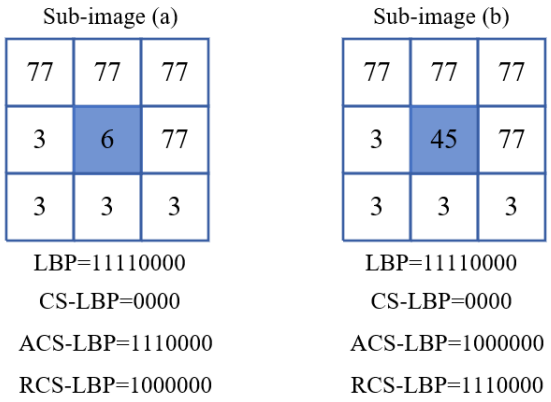

FIGURE 1. Illustration of the code of LBP, CS-LBP, ACS-LBP and RCS-LBP patterns of central pixels in the two sub-images.

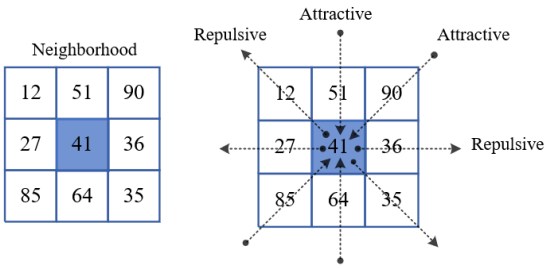

FIGURE 2. Example of attractive-and-repulsive micro-structures along with the vertical and horizontal directions, and the two diagonal directions.

center-symmetric pairs of the pixels in the local window is expressed. Thus more stable results and texture modeling were obtained. The proposed methods are similar to LCvMSP and LCxMSP methods. However, ACS-LBP and RCS-LBP methods compare the same four pairs of center-symmetric pixels with the value of the center pixel. The Attractive and Repulsive Binary Thresholding Functions (ABTF and RBTF) kernel functions were used for this comparison. The ABTF kernel function is defined as in Eq. (5) [51].

$$\begin{aligned} \xi(g_i, g_c, g_j) &= \rho(g_i, g_c) \otimes \rho(g_j, g_c) \\ &= \begin{cases} 1, & if\ g_i \geq g_c\ and\ g_j \geq g_c \\ 0, & otherwise \end{cases} \end{aligned} \tag{5}$$

where g_c represents the gray value of the central pixel, g_i and g_j represent the gray values of the neighboring pixels of the central pixel. The RBTF kernel function is defined as in Eq. (6) [51].

$$\begin{aligned} \zeta(g_i, g_c, g_j) &= \overline{\rho}(g_i, g_c) \otimes \overline{\rho}(g_j, g_c) \\ &= \begin{cases} 1, & if\ g_i \leq g_c\ and\ g_j \leq g_c \\ 0, & otherwise \end{cases} \end{aligned} \tag{6}$$

Fig. 2 shows neighborhood relations of ACS-LBP and RCS-LBP methods. As seen in Fig. 2, the methods express the four triple neighborhood relations, namely horizontal, vertical and two diagonal directions. These methods also

model the relationship of these pixels to the center pixel using three virtual pixels. The first virtual pixel is the local median value (λ) calculated over the 3×3 neighborhood of the central pixel. The other two virtual pixels are the average value of the entire image and the average gray-scale value of the sub-image taken in 3×3 dimensions. A total of four triple neighborhood relationships, horizontal, vertical and two diagonal, and virtual pixels are compared with the central pixel using the Heaviside step function $\rho(.)$. There is no need to define any threshold value in these methods. The ACS-LBP and RCS-LBP features are computed in the following form using both the ξ and ζ kernel functions and the Heaviside step function ρ [51].

$$ACS - LBP_{3\times3}(\times) = \mathrm{w}_7^{\mathrm{T}} g_{ACS-LBP} \tag{7}$$
$$RCS - LBP_{3\times3}(\times) = \mathrm{w}_7^{\mathrm{T}} g_{RCS-LBP} \tag{8}$$

In Eqs. (7) and (8), superscript $^{\mathrm{T}}$ and w_7 denotes the transpose operation and a vector of weighting factors, respectively. w_7 vector is chosen arbitrarily and it is defined as in Eq.(9).

$$\mathrm{w}_7^{\mathrm{T}} = \left[2^6\ 2^5\ 2^4\ 2^3\ 2^2\ 2^1\ 2^0\right] \tag{9}$$

The kernel functions defined in Eqs. (7) and (8) can be rewritten as follows [51]

$$\begin{aligned} ACS - LBP(x_c, y_c) = &\sum_{p=0}^{\frac{P}{2}-1} \xi(g_p, g_c, g_{p+P/2}) \times 2^p \\ &+ \rho\left(\frac{1}{P+1}\left(\sum_{p=0}^{P-1} g_p + g_c\right), g_c\right) \times 2^{P/2} \\ &+ \rho\left(\frac{\sum_{m=1}^{M}\sum_{n=1}^{N} I(m,n)}{M \times N}, g_c\right) \times 2^{(P/2)+1} \\ &+ \rho(\lambda, g_c) \times 2^{(P/2)+2} \end{aligned} \tag{10}$$

$$\begin{aligned} RCS - LBP(x_c, y_c) = &\sum_{p=0}^{\frac{P}{2}-1} \zeta(g_p, g_c, g_{p+P/2}) \times 2^p \\ &+ \rho\left(g_c, \frac{1}{P+1}\left(\sum_{p=0}^{P-1} g_p + g_c\right)\right) \times 2^{P/2} \\ &+ \rho\left(g_c, \frac{\sum_{m=1}^{M}\sum_{n=1}^{N} I(m,n)}{M \times N}\right) \times 2^{(P/2)+1} \\ &+ \rho(g_c, \lambda) \times 2^{(P/2)+2} \end{aligned} \tag{11}$$

where, x_c and y_c represent the coordinates of the central pixel g_c, while $g_p (p \in \{0, 1, \ldots, P-1\})$ denotes the grayscale values of the peripheral pixels. k represents the number of ACS-LBP and RCS-LBP patterns. ACS-LBP and RCS-LBP labels are generated for all pixels of the image, and then histograms representing the texture are generated as in Eqs. (12) and (13) [51].

$$h_{ACS-LBP}(k) = \sum_x \sum_y \delta(ACS - LBP(x, y), k) \tag{12}$$
$$h_{RCS-LBP}(k) = \sum_x \sum_y \delta(RCS - LBP(x, y), k) \tag{13}$$

IV. PROPOSED METHOD

The effective texture analysis can be carried out by using different characteristics of texture images. In particular, the differential features in different scales and directions are less affected by rotation and noise conditions. In this study, a novel LBP method has been developed using the statistical texture analysis capabilities of the ACS-LBP method which is one of the up-to-date LBP methods and differential texture information of the Hessian matrix together. In the literature works, eigenvalues of the Hessian matrix were used to improve the classification performance of LBP models [47]. However, as far as we know, this work is the first in applying magnitude information of the Hessian matrix to state-of-the-art LBP models by means of multi-scale analysis for texture classification. Similar to the coding strategy of ACS-LBP, the Hessian matrix is converted into a binary string and $Hess^{\sigma}_{P,R}$ denotes the binary map. The proposed LBP based method is called Hess-ACS-LBP. The ACS-LBP and $Hess^{\sigma}_{P,R}$ are joined to form a 2-D joint feature histogram. The proposed method doesn't contain any preprocessing algorithm such as normalization and filtering. Initially, the input image is converted from RGB to grayscale before processing. Then Hessian matrix and LBP features are calculated on grayscale images. The LBP features and Hessian matrix of input image are computed and used together to perform multi-resolution texture analysis. Our Hess-ACS-LBP descriptor and its multiresolution framework are shown in Fig. 3. The proposed Hess-ACS-LBP method consists essentially of three steps: (1) calculation of Hessian matrix and rotation invariant uniform LBP features, (2) independent constructions of Hess-ACS-LBP descriptor, (3) cross-scale joint coding and texture classification.

A. CALCULATION OF HESSIAN MATRIX

In mathematics, the Hessian matrix is a square matrix of second-order partial derivatives of a scalar-valued function. Let $f(x)$ be the intensity function of an I image. For the (x, y) pixel point of a 2-D image, the Hessian matrix of the image is defined as in Eq. (14).

$$H(I(x,y)) = \begin{bmatrix} I_{xx} = \dfrac{\partial^2 I(x,y)}{\partial x^2} & I_{xy} = \dfrac{\partial^2 I(x,y)}{\partial x \partial y} \\ I_{yx} = \dfrac{\partial^2 I(x,y)}{\partial x \partial y} & I_{yy} = \dfrac{\partial^2 I(x,y)}{\partial y^2} \end{bmatrix} \tag{14}$$

where I_{xx}, I_{xy}, I_{yx} and I_{yy} express the four second-order partial derivatives of the original 2-D image. Gaussian derivative filters are used to compute the Hessian matrix of the image.

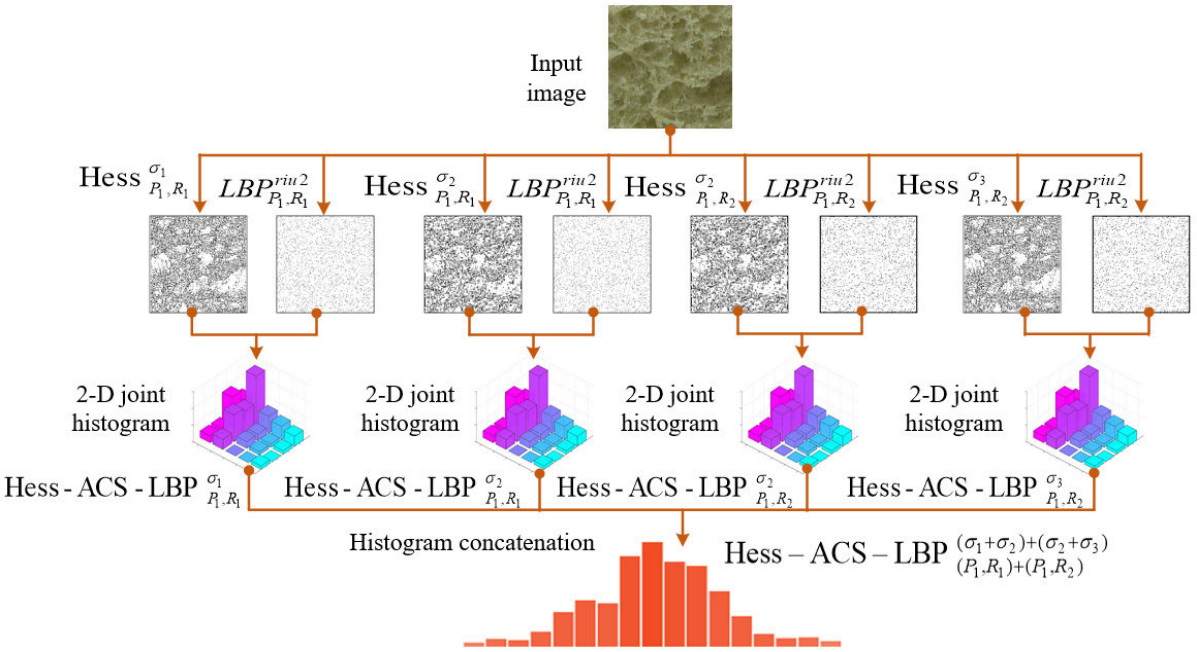

FIGURE 3. The flowchart of the proposed Hess-ACS-LBP method with cross-scale joint coding.

The Gaussian function is given as [20]:

$$G(x, y, \sigma) = \frac{1}{2\pi\sigma^2} \exp(\tfrac{x^2+x^2}{2\sigma^2}) \tag{15}$$

Second-order horizontal, vertical and diagonal derivatives of Gaussian function are defined as:

$$G_{xx} = \frac{1}{2\pi\sigma^4}\left(\frac{x^2}{\sigma^2} - 1\right) e^{(-\frac{x^2+y^2}{2\sigma^2})} \tag{16}$$

$$G_{xy} = \frac{xy}{2\pi\sigma^6} e^{(-\frac{x^2+y^2}{2\sigma^2})} \tag{17}$$

$$G_{yy} = \frac{1}{2\pi\sigma^4}\left(\frac{y^2}{\sigma^2} - 1\right) e^{(-\frac{x^2+y^2}{2\sigma^2})} \tag{18}$$

The horizontal, vertical and diagonal derivatives of the gray-level texture images are calculated by convolution as follows:

$$I_{xx} = I * G_{xx} \tag{19}$$

$$I_{xy} = I * G_{xy} \tag{20}$$

$$I_{yy} = I * G_{yy} \tag{21}$$

B. CONSTRUCTION OF HESS-ACS-LBP DESCRIPTOR

The differential information of the Hessian matrix can be used with different computations to provide valuable information about the image surface [52]. In literature, the maximum and minimum curvature directions of the pixel points can be determined with the eigenvalues and eigenvectors of the Hessian matrix extensively [48]. Thus, local structural features of the image can be obtained. The structural feature of the image has been analyzed according to the relationship between the eigenvalues of the Hessian matrix. Then the image surface is classified and distinctive points are determined according to the sign of the eigenvalues. Besides, the geometric structures of pixels can be analyzed using a trace with the determinant of the Hessian matrix [18]. Therefore, information such as curvature, multi-scale image derivative and surface type, which provides highly distinctive information from the Hessian matrix, was used in image analysis. The overview of the proposed method is shown in Fig. 3.

In this study, texture analysis was carried out using up-to-date LBP method with the Hessian matrix which has strong differential information hybridly. 2-D joint histogram was obtained by using magnitude which is obtained from the Hessian matrix together with ACS-LBP method. The I_{xx} and I_{yy} obtained from the Hessian matrix calculated in Eq. (14) are the second-order horizontal and vertical derivative on the scale σ. The magnitude is computed for a texture image and it is shown in Fig. 4. In this study, the magnitude of the image is computed only with the second-order horizontal and vertical derivatives of the Hessian matrix as shown in Eq. (22).

$$Mag = \sqrt{I_{xx}^2 + I_{yy}^2} \tag{22}$$

To encode the $LBP^{riu2}_{P,R}$ and Mag hybridly and distinctly, the operator in the ACS-LBP method was used [51]. However, unlike the ACS-LBP method, the magnitude (Mag) which computed from the Hessian matrix is used in the following form:

$$Hess - ACS - LBP(x_c, y_c)^{\sigma}_{P,R} = \sum_{p=0}^{\frac{P}{2}-1} \xi(g_p, g_c, g_{p+P/2}) \times 2^p$$

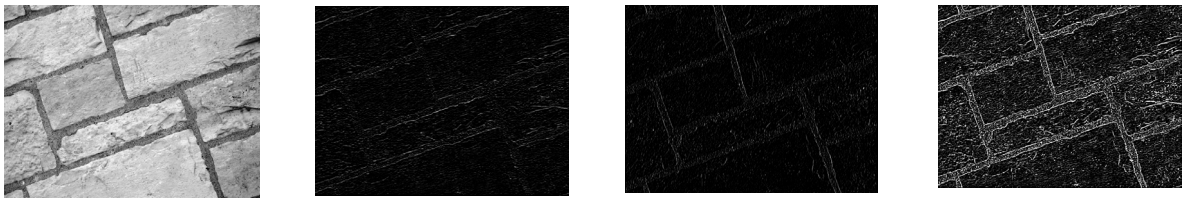

FIGURE 4. The magnitude information of the texture image with Gaussian standard deviation $\sigma = 1$.

$$+\rho\left(\frac{1}{P+1}\left(\sum_{p=0}^{P-1} g_p + g_c\right), g_c\right) \times 2^{P/2} + \rho\left(\frac{\sum_{m=1}^{M}\sum_{n=1}^{N} Mag(m,n)}{M \times N}, g_c\right) \times 2^{(P/2)+1} + \rho(\lambda, g_c) \times 2^{(P/2)+2} \quad (23)$$

There is a significant difference between Eq. (10) in section 2 and Eq. (23) used in the proposed method. The equation in the ACS-LBP method uses the Attractive Binary Thresholding Function ($\xi(.)$) to calculate local pixel neighborhoods through input texture image. In our method, local pixel neighborhoods are encoded by the *Mag* instead of input image. Thus, the Hessian of the image is actively used to reveal the relationship between the center pixel and the peripheral pixel. Thanks to the distinctive local difference information which is provided by the Hessian matrix, distinguishing pixel differences were obtained. It should be pointed that ABTF kernel function in Eq. (23) uses the magnitude *Mag* to compare the same four pairs of center-symmetric pixels with the value of the center pixel. Heaviside step function $\rho(.)$ also uses the magnitude *Mag* to extract four triple neighborhood relationships compared with the central pixel in the same way. Furthermore, the proposed method does not require any threshold parameter, similar to ACS-LBP method. The Hessian matrix is calculated in a multi-scale structure and the responses of the different derivative filters in the image are obtained. Thus, the microstructures in the horizontal and vertical directions are revealed.

Similar to $LBP^{riu2}_{P,R}$, $Hess-\text{ACS-LBP}(x_c, y_c)^{riu2\_\sigma}_{P,R}$ corresponds to the rotation-invariant pattern of $Hess-\text{ACS-LBP}(x_c, y_c)^{\sigma}_{P,R}$. In this study, the proposed $Hess-\text{ACS-LBP}(x_c, y_c)^{riu2\_\sigma}_{P,R}$ operator is used with $LBP^{riu2}_{P,R}$ operator. Thus, the joint information of the $Hess-\text{ACS-LBP}(x_c, y_c)^{riu2\_\sigma}_{P,R}$ and $LBP^{riu2}_{P,R}$ is encoded. As a result, a 2-D joint histogram is generated, denoted by *Hess-ACS-LBP*.

C. CROSS-SCALE JOINT CODING AND REPRESENTATION

The high classification accuracy can be achieved using multi-resolution texture analysis. Three different Gaussian derivative filters are used to compute the Hessian matrix of the texture image. The diameter of these filters is determined by the Gaussian standard deviation σ value. The microstructures of the image in horizontal and vertical directions can be obtained at the pixel level when the σ value is selected in the appropriate range. In this study, the magnitude with three different σ values was used in a cross-scale structure with the rotation-invariant uniform local binary pattern ($LBP^{riu2}_{P,R}$) method. The multi-resolution texture analysis was carried out with different (P, R) and σ values. To reduce the feature vector size of the proposed Hess-ACS-LBP method, only the radius R and Gaussian standard deviation σ values were modified. The value of the sampling neighborhood P is chosen as 8. The x_c and y_c, in Eq. (23), which denote the coordinates of the central pixel g_c, are not shown in the following steps. The cross-scale joint coding is performed as follows:

1) $LBP^{riu2}_{P,R}$ and $Hess-\text{ACS-LBP}(x_c, y_c)^{riu2\_\sigma}_{P,R}$ with (P_1, R_1) and σ_1 are joined. The obtained result is denoted as $Hess-\text{ACS-LBP}^{\sigma_1}_{P_1,R_1}$.
2) In $Hess-\text{ACS-LBP}^{\sigma_1}_{P_1,R_1}$, σ_1 value is replaced by σ_2, and the new term is denoted as $Hess-\text{ACS-LBP}^{\sigma_2}_{P_1,R_1}$.
3) These two variants are combined in concatenation and the result is defined as $Hess-\text{ACS-LBP}^{(\sigma_1+\sigma_2)}_{P_1,R_1}$.
4) Similar to step 2 and 3, another variant with (P_1, R_2), σ_2 and σ_3 is obtained, and it is denoted by $Hess-\text{ACS-LBP}^{(\sigma_3+\sigma_2)}_{P_1,R_2}$.
5) $Hess-\text{ACS-LBP}^{(\sigma_1+\sigma_2)}_{P_1,R_1}$ and $Hess-\text{ACS-LBP}^{(\sigma_3+\sigma_2)}_{P_1,R_2}$ are further concatenated to construct the multiresolution scheme. This scheme is denoted by $Hess-\text{ACS-LBP}^{(\sigma_1+\sigma_2)+(\sigma_3+\sigma_2)}_{(P_1,R_1)+(P_1,R_2)}$.

V. EXPERIMENTAL RESULTS

In order to demonstrate the effectiveness of the proposed Hess-ACS-LBP method in the texture classification problem, two different experimental studies were carried out on varied datasets. The first experimental study was carried out on commonly used texture databases. The second experiment was carried out on texture databases that contain a lot of classes. Thus, the effectiveness of the proposed method in texture classification problems involving numerous classes was realized.

The nearest neighbor classifier (1-NN) is used to demonstrate the distinctive power of the proposed method. 1-NN is a non-parametric classifier, and it is suitable for comparison purposes [44]. The accuracy evaluation metric is used to compare the similarity and diversity of the predicted and true

TABLE 1. Summary of the texture datasets used in experiments.

No.	Name	Classes	Samples per class	Total samples	Sample resolution
A	CUReT	61	92	5612	200 × 200
B	USPTex	191	12	2292	128 × 128
C	KTH-TIPS2b	11	16	176	100 × 100
D	MondialMarmi	12	64	768	136 × 136
E	OuTeX TC_00013	68	20	1360	128 × 128
F	XU HR	25	40	1000	1280 × 960
G	ALOT	250	110	27500	512 × 768
H	STex	476	16	7616	128 × 128

label sets. Average accuracy is defined as follows [53]:

$$accuracy = \frac{1}{p}\sum_{i=1}^{p}\frac{TP_i + TN_i}{TP_i + TN_i + FP_i + FN_i} \tag{24}$$

where TP, FP, FN, TN and p denote the number of true positives, false positives, false negatives, true negatives and total number of classes respectively. Chi-square distance is used to compute the similarity between test and training histograms [14]. Using Chi-square distance and 1-NN, the distance between two histograms is defined as in Eq. (25).

$$D(U, V) = \sum_{i=1}^{N}(U_i - V_i)^2/(U_i + V_i) \tag{25}$$

where N denotes the number of histogram bins, U_i and V_i denotes the values at the i-th bin of the histograms of the original and assigned images, respectively.

A. TEXTURE DATASETS

The CUReT [54], USPTex [55], KTH-TIPS2b [56], Mondial-Marmi [57], Outex_TC_00013 [58] and XU HR [59] datasets were used in the first of our experiences. The CUReT dataset contains 61 texture classes and each class has 205 instances. The USPTex dataset contains different color texture images such as rice, vegetation and cloud. It consists of a total of 2292 texture images, 191 classes and 12 samples in each class. KTH-TIPS2b dataset contains textures obtained under different lighting, scale and pose conditions. KTH-TIPS2b dataset has 11 texture classes with 432 samples per class. MondialMarmi dataset contains the color images of granite. It has 12 classes with 64 samples per class. The images have been obtained under controlled illumination conditions and 9 rotation angles. Outex_TC_00013 dataset contains 68 texture classes. XU HR dataset has 25 texture classes with 40 high-resolution images per class. This dataset has viewpoint changes, scale differences and non-rigid deformations between different samples of the same class. In the second stage of the experimental studies, datasets containing a lot of texture classes and less used than other data sets were used. The ALOT dataset [60] is a 250-class dataset with different viewpoints, illumination angles and illumination color changes. It consists of more than 27500 images and

FIGURE 5. Sample texture images from (a) Stex (b) ALOT databases.

uses different light source colors. STex dataset has 476 color texture images [61]. It consists of more texture images than VisTex [62] and Brodatz datasets [63]. In this paper, we use STex-512-splitted package. It contains 7616 color texture images of size 128 × 128. The main properties of each dataset are given in detail in Table 1. 70% and 30% of the images in the datasets were used for training and testing respectively. However, to make fair comparison in Table 7, half of the samples in each dataset (for each class) were randomly selected for training and the remaining half for testing as in [51]. Some texture samples used in our experiments are shown in Fig. 5 and 6.

B. PARAMETERS SELECTION AND ANALYSIS

The proposed method $Hess - ACS - LBP^{\sigma}_{P,R}$ contains 3 parameters. These are sampling neighborhood P, Gaussian standard deviation σ and sampling radius R. In this study,

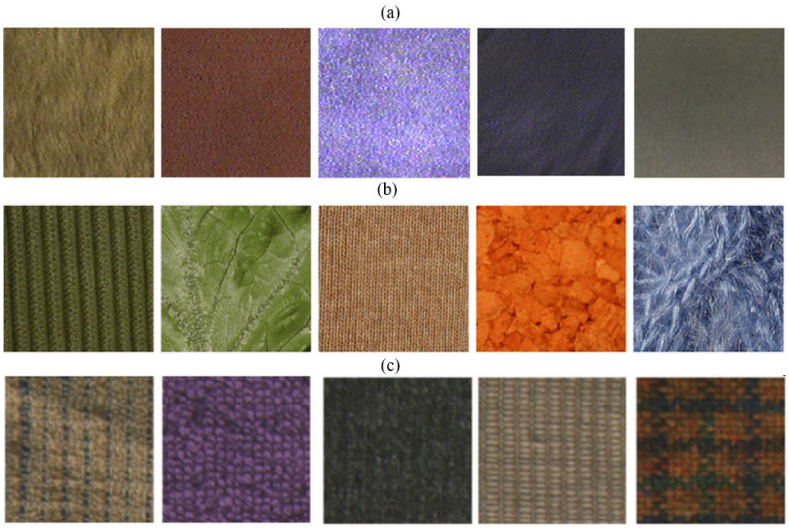

FIGURE 6. Texture image examples from (a) CUReT (b) KTH-TIPS2-b (c) Outex TC_00013 datasets.

TABLE 2. Experimental results of the proposed descriptor with different σ on XU HR Dataset.

$Hess-ACS-LBP^{\sigma}_{P,R}$	$\sigma=0.25$	$\sigma=0.5$	$\sigma=1$	$\sigma=1.5$	$\sigma=2$	$\sigma=3$	$\sigma=4$
(P,R)=(8,1)	92.76	93.79	94.14	95.17	**96.55**	96.21	95.52
(P,R)=(8,2)	96.55	**97.93**	95.52	94.14	95.17	94.83	93.79
(P,R)=(8,3)	**96.90**	96.21	**97.24**	95.86	95.52	95.52	94.83
(P,R)=(8,4)	96.55	95.86	**96.90**	96.21	95.52	95.17	94.14
(P,R)=(8,5)	**97.24**	**97.24**	96.21	96.21	**96.90**	96.55	94.14

$P = 8$ is fixed to shorten the feature vector size. However, using the Gaussian standard deviation σ and LBP sampling radius R parameters in the design of derivative filters, the classification accuracy of the proposed method was evaluated. The evaluation of parameters was given using XU HR dataset.

Derivative filters designed using Gaussian function are used in the calculation of the Hessian matrix. The radius of these filters is determined by Gaussian standard deviation σ. If the σ value is selected too small, the derivative information will be sensitive to noise. Derivative filters designed using a larger σ value can ignore important fluctuations such as texture details and edge-to-corner. In this study, the optimal values of σ value were analyzed experimentally and multi-scale texture analysis was carried out. In different experimental studies, different σ values ranging from 0.25 to 4 were analyzed. The effect of different parameters on classification performance was analyzed using XU HR dataset. Firstly, the effects of different σ values on the proposed $Hess - ACS - LBP^{\sigma}_{P,R}$ method were evaluated. As seen in Table 2, the best results were obtained with $\sigma = 0.5$ and 1. However, among the other σ values, significant results were obtained.

The classification performance of LBP features with two different σ values was observed using $Hess-\text{ACS-LBP}^{\sigma_1+\sigma_2}_{P,R}$ feature which composes of $Hess - \text{ACS-LBP}^{\sigma_1}_{P,R}$ and $Hess - \text{ACS-LBP}^{\sigma_2}_{P,R}$ features. As seen from Table 3, the best results are obtained when σ_1 is 0.5 and σ_2 is 1, 1.5 and 2. Furthermore, when the sampling neighborhood $P = 8$ and the sampling radius $R = 3$, the specified σ values gives promising results. Since the Hessian matrix is calculated for different σ values, a multi-scale analysis of the texture image is performed. The differential information in this study is evaluated with different neighborhood and radius values and pixel relationships are discovered.

The third analysis was performed to observe the effect of both two different σ values and two different radius. The $Hess - ACS - LBP^{(\sigma_1+\sigma_2)}_{(P_1,R_1)+(P_1,R_2)}$ feature vector consists of two different radius and σ values $Hess - ACS - LBP^{(\sigma_1+\sigma_2)}_{(P_1,R_1)}$ and $Hess-ACS-LBP^{(\sigma_1+\sigma_2)}_{(P_1,R_2)}$. Table 4 shows the classification results of $Hess-ACS-LBP^{(\sigma_1+\sigma_2)}_{(P_1,R_1)+(P_1,R_2)}$ features. Generally, the best results were obtained with $(P_1, R_1) + (P_1, R_2) = (8, 1) + (8, 4)$ and $(8, 3) + (8, 5)$ parameters.

TABLE 3. Experimental results (%) of the $Hess-ACS-LBP_{P,R}^{(\sigma_1+\sigma_2)}$ descriptor on XU HR Dataset.

$Hess-ACS-LBP_{(P,R)}^{(\sigma_1+\sigma_2)}$	$\sigma_1=0.5$	$\sigma_1=0.5$	$\sigma_1=0.5$	$\sigma_1=1$	$\sigma_1=1$	$\sigma_1=1.5$
	$\sigma_2=1$	$\sigma_2=1.5$	$\sigma_2=2$	$\sigma_2=1.5$	$\sigma_2=2$	$\sigma_2=2$
(P,R)=(8,1)	95.52	95.52	95.86	94.14	95.52	96.21
(P,R)=(8,2)	97.24	95.52	95.86	95.17	95.17	94.14
(P,R)=(8,3)	**98.28**	**97.59**	**98.28**	97.59	97.24	96.55
(P,R)=(8,4)	96.90	**97.59**	**97.59**	97.24	96.55	97.24
(P,R)=(8,5)	96.21	96.90	96.21	96.90	96.21	96.90

TABLE 4. Experimental results (%) of the $Hess-ACS-LBP_{(P_1,R_1)+(P_1,R_2)}^{(\sigma_1+\sigma_2)+(\sigma_3+\sigma_2)}$ descriptor on XU HR Dataset.

$Hess-ACS-LBP_{(P_1,R_1)+(P_1,R_2)}^{(\sigma_1+\sigma_2)+(\sigma_3+\sigma_2)}$	$\sigma_1=0.5$	$\sigma_1=0.5$	$\sigma_1=0.5$	$\sigma_1=0.5$	$\sigma_1=0.5$	$\sigma_1=1$	$\sigma_1=1$	$\sigma_1=1.5$	$\sigma_1=1.5$	$\sigma_1=1$
	$\sigma_2=1$	$\sigma_2=1$	$\sigma_2=1.5$	$\sigma_2=1.5$	$\sigma_2=2$	$\sigma_2=0.5$	$\sigma_2=0.5$	$\sigma_2=0.5$	$\sigma_2=1$	$\sigma_2=2$
	$\sigma_3=1.5$	$\sigma_3=2$	$\sigma_3=2$	$\sigma_3=2$	$\sigma_3=1$	$\sigma_3=1.5$	$\sigma_3=2$	$\sigma_3=2$	$\sigma_3=2$	$\sigma_3=1.5$
(P,R)=(8,1) (P,R)=(8,4)	98.89	98.52	**98.89**	99.26	98.52	**98.89**	**99.26**	**99.26**	98.89	**99.26**
(P,R)=(8,3) (P,R)=(8,4)	99.26	99.26	**99.26**	98.89	99.26	**98.89**	**99.26**	**99.26**	98.52	**98.52**
(P,R)=(8,3) (P,R)=(8,5)	99.26	99.26	**99.26**	98.89	99.26	**99.63**	**99.63**	**98.89**	98.89	**98.52**
(P,R)=(8,4) (P,R)=(8,5)	**99.26**	**99.26**	**99.63**	**98.52**	**99.26**	**99.26**	**99.26**	**99.63**	**98.52**	**98.15**

In the last parameter analysis, the classification behavior of $Hess-ACS-LBP_{(P_1,R_1)+(P_1,R_2)}^{(\sigma_1+\sigma_2)+(\sigma_2+\sigma_3)}$ feature was observed from different ways. Adjacency and radius analysis was carried out with 3 different σ values and classification performance was evaluated. As seen in Table 5, the $Hess-ACS-LBP_{(P_1,R_1)+(P_1,R_2)}^{(\sigma_1+\sigma_2)+(\sigma_2+\sigma_3)}$, $Hess-ACS-LBP_{(P_1,R_1)+(P_1,R_2)}^{(\sigma_1+\sigma_2)}$ descriptor obtained similar accuracy results. These results show that analyzes using more σ values have no significant effect on classification accuracy. When all the results were examined in general, it was found that the descriptors obtained with two different σ and radius values give better results than single σ and radius values.

C. COMPARATIVE PERFORMANCE ASSESSMENT

The proposed Hess-ACS-LBP method was compared with the up-to-date LBP methods on 6 different datasets. Experimental results are given in Table 7. The results of the compared methods were taken from the original paper. The proposed Hess-ACS-LBP method has the highest classification accuracy in all datasets. The most important point in the proposed method is the utilization of Hessian matrix in a multi-scale manner. The distinctive 2-D joint histogram was constructed using the Hessian magnitude hybridly with the ACS-LBP method in [51]. The generated histograms were concatenated and texture representation was accomplished. Therefore, the texture analysis power of ACS-LBP method is combined with the Hessian information to capture second-order textural changes in the image. Thanks to multi-resolution approach, information such as edges and corners that express textural changes are represented in histogram information. As seen in Table 7, the proposed hybrid approach has achieved better results than the ACS-LBP method in all datasets. The proposed method also obtained better results than the ARCS-LBP method, in which ACS-LBP and RCS-LBP method are combined. The classification accuracy in all datasets was increased about between 2% and 11%. Especially on USPTex dataset, the classification accuracy was increased by 11% compared to other methods. Besides the different neighborhood and radius values used in the proposed method, the horizontal and vertical derivative information obtained from the Hessian matrix provided information in the analysis of rotated images.

The microstructures of texture pixels were revealed out by multi-scale analysis using the magnitude obtained from

TABLE 5. Experimental results (%) of the Hess − ACS − $LBP^{(\sigma_1+\sigma_2)}_{(P_1,R_1)+(P_1,R_2)}$ descriptor on XU HR Dataset.

Hess−ACS−$LBP^{(\sigma_1+\sigma_2)}_{(P_1,R_1)+(P_1,R_2)}$	$\sigma_1=0.5$ $\sigma_2=1$	$\sigma_1=0.5$ $\sigma_2=1.5$	$\sigma_1=0.5$ $\sigma_2=2$	$\sigma_1=1$ $\sigma_2=1.5$	$\sigma_1=1$ $\sigma_2=2$	$\sigma_1=1.5$ $\sigma_2=2$
(P,R)=(8,1) (P,R)=(8,2)	97.78	98.89	98.52	97.41	97.78	98.15
(P,R)=(8,1) (P,R)=(8,3)	98.15	98.52	98.52	98.52	98.52	**99.26**
(P,R)=(8,1) (P,R)=(8,4)	98.89	**99.26**	**99.26**	98.52	98.89	**99.63**
(P,R)=(8,1) (P,R)=(8,5)	98.89	98.89	**99.26**	98.89	98.89	**99.26**
(P,R)=(8,2) (P,R)=(8,3)	**99.26**	98.15	98.89	97.04	98.15	98.89
(P,R)=(8,2) (P,R)=(8,4)	98.89	98.52	98.89	98.52	98.89	**99.26**
(P,R)=(8,2) (P,R)=(8,5)	98.52	98.52	**99.26**	98.89	98.89	**99.26**
(P,R)=(8,3) (P,R)=(8,4)	98.89	**99.63**	**99.26**	98.52	98.52	98.52
(P,R)=(8,3) (P,R)=(8,5)	**99.63**	**99.26**	**99.26**	98.89	98.52	98.52
(P,R)=(8,4) (P,R)=(8,5)	**99.26**	**99.63**	**98.89**	**98.52**	**98.52**	**98.15**

the Hessian matrix in Eq. (22). When σ_1 is chosen as 0.5 and σ_2 is chosen as 1, 1.5 and 2, pixel fluctuation behavior at micro-level can be computed with a multi-scale approach. The positive effects of the multi-scale approach were observed in discrimination of in-class and inter-class similarity information in datasets. Thus, this situation has an effect on high classification accuracy especially on CURet and KTH-TIPS2b dataset.

D. THE EFFECTIVENESS OF THE PROPOSED METHOD ON DATASETS WITH A HIGH NUMBER OF CLASSES

The effectiveness of the proposed hybrid LBP method has been evaluated on datasets with a high number of classes such as ALOT and STex. In the literature, the desired classification accuracy could not be obtained on these datasets. The high number of classes and the similarity between the classes undermine the discrimination of methods. Table 6 gives the comparison of the proposed methods and the state-of-the-art methods on the two-color datasets. The proposed method was compared with both traditional texture analysis methods and deep learning methods. As seen from Table 6, the traditional LBP method yields 39.57% and 54.89% results in ALOT and STex datasets, while the proposed Hess-ACS-LBP method achieves 97.20% and 92.60% classification results, respectively. Deep learning methods have achieved better results on datasets than traditional methods. However, the proposed Hess-ACS-LBP method has achieved better results than deep learning methods. The Hess-ACS-LBP method, which codes geometric changes of texture information, revealed the effect of pixel changes on the texture detaily. The ResNet101 and ResNet50 methods yielded successful results in the STex dataset but yielded low results in the ALOT dataset.

As a conclusion, intra-class and inter-class textural structure could differentiate from both irrelevant background and other texture types by multiscale Hessian analysis. During the experimental studies, we noticed that there were some background responses in the magnitude image, which calculated from the Hessian matrix. To avoid these background artifacts, the multiscale Hessian scheme is used. Hessian matrix is adapted in the LBP methodology, in which it is calculated pixel by pixel for obtaining most relevant features such as edge, corner and texture primitives. The most relevant features in the texture regions are calculated for various sigma values. Therefore, integrating the most relevant features and LBP features can achieve structure-aware texture classification.

VI. DISCUSSION

The results in section V shows that the proposed method achieves better results in the texture classification for all datasets. Although the databases used in experimental studies

TABLE 6. The comparison of the proposed methods and the state-of-the-art methods on the two color databases ALOT (250) and STex (476).

Texture descriptor	Datasets	
	ALOT (250)	STex (476)
LBP [14]	39.57	54.89
CLBP [64]	49.6	58.4
CIF-LBP [65]	–	40.95
CIF-LBP-PSO [65]	–	45.61
DWT-Gamma-KLD [66]	40.7	52.90
Gaussian-copula-Weibull-ML [67]	54.10	70.06
Student t Copula Gamma-ML [67]	47.5	64.3
Multivar. Power Exp. [68]	49.3	71.3
ODBTC [69]	43.62	–
DDBTC [70]	48.64	44.79
LECoP [71]	–	74.15
LED+RD [72]	–	80.08
AlexNet [73]	59.01	68.32
VGG16 [74]	60.34	72.16
VGG19 [74]	59.15	71.68
GoogleNet [75]	60.71	77.60
ResNet101 [76]	75.60	91.18
ResNet50 [76]	75.68	91.59
OWT-MDCM [77]	48.13	72.28
DTCWT-MDCM [77]	55.74	77.01
Gabor-MDCM [77]	60.36	83.36
MWavelets-MDCM [77]	61.88	85.46
Our Hess-ACS-LBP	**97.20**	**92.60**

include many image transformations such as rotation, scaling and viewpoint, the proposed method was able to deal with these situations. Especially the XU HR dataset consists of many of these transformations. However, since the proposed Hess-ACS-LBP method is constructed with different σ and R values, it has achieved a very high classification accuracy (99.6%) on the XU HR database. The σ parameter has critical importance for the Hess-ACS-LBP method. The local changes should be captured for interpretation of textural primitives in texture images. The Hessian matrix expresses these local changes. However, different σ parameters should be used to detect micro-level changes. While the local changes are captured with these parameters, scale-invariant texture representation is performed. Table 2-5 show the classification results of both LBP and local second-order image components by using 7 different σ and 5 different R values crosswise. In the detailed parameter analysis, the effect of each parameter was examined and optimal parameters were determined.

Another point to be emphasized is that each of the Hessian matrices calculated with different σ values combined with the features and provided to be complementary for each other. Table 7 expresses this situation. For example, the traditional LBP method has a 91.03% and 79.06% classification accuracy on the CUReT and MondialMarmi databases, while the ACS-LBP method has a 94.72% and 91.99% classification accuracy, respectively. The proposed Hess-ACS-LBP method has 97.06% and 100% classification accuracy. The difference between results is remarkable. As seen in Table 6, the proposed method has achieved remarkable results in datasets with high number of classes. It is clear that the feature extraction procedure is the basis of this performance. Because the proposed method provides stable learning to classifier even in datasets with high number of classes.

Although the developed method has high accuracy results, it is also in a very convenient position in terms of computational cost. It is clearly seen in Fig. 7. We compare the average running time of different methods to calculate one image descriptor by running on a PC with an Intel Core i5-7400 CPU and 8GB RAM. The LBP [14], RALBGC [44], LPQ [102], LCvMSP [43], LDTP [80], LCxMSP [43], LDN [22], MRELBP [30], PCLBP [45],

TABLE 7. Comparison of proposed method with the state-of-the-art LBP methods.

Texture descriptor	Ref.	Dataset					
		A	B	C	D	E	F
Hess-ACS-LBP	This paper	**96.9**	**98.9**	**97.9**	**100**	**94.5**	**98.8**
ARCS-LBP	El merabet et al. [51]	94.72	88.88	93.61	91.99	85.72	97.21
ACS-LBP	El merabet et al. [51]	94.29	87.66	93.28	90.73	84.17	97.19
RCS-LBP	El merabet et al. [51]	94.02	87.45	92.76	89.92	84.88	97.09
LCCMSP	El merabet and Ruichek [43]	94.92	90.01	93.51	90.46	84.78	96.48
LCvMSP	El merabet and Ruichek [43]	94.22	88.88	93.08	89.98	83.87	96.15
LCxMSP	El merabet and Ruichek [43]	94.48	88.48	91.85	88.01	84.23	96.34
RALBGC	El-khadiri et al. [44]	94.35	87.71	93.95	90.07	83.06	95.34
RLBGC	El-khadiri et al. [44]	93.19	85.70	93.66	87.74	82.05	95.27
ALBGC	El-khadiri et al. [44]	93.87	85.82	93.53	86.85	80.90	94.45
CELDP	Faraji and Qi [78]	76.46	80.61	86.70	85.79	81.02	89.55
DSLGS	Dong et al. [79]	94.54	81.15	87.07	82.45	81.78	92.62
LDTP	Rivera et al. [80]	84.78	76.23	88.00	81.80	72.70	89.61
AHP	Zhu et al. [81]	93.69	84.88	90.64	87.60	80.79	96.20
OTF	Xu et al. [82]	67.71	35.89	56.53	40.96	46.88	93.06
LNDP	Verma and Raman [83]	91.64	80.66	87.85	80.27	77.16	90.42
LQPAT	Chakraborty et al. [84]	91.43	78.32	84.25	81.31	76.87	90.09
LDENP	Pillai et al. [85]	69.26	50.12	71.52	65.11	67.96	76.08
mdLBP	Dubey et al. [86]	90.90	82.51	88.48	81.01	78.35	91.40
maLBP	Dubey et al. [86]	90.90	82.51	88.48	81.01	78.35	91.40
NI/LBP	Liu et al. [87]	83.14	70.50	81.51	80.72	76.25	85.52
NI/RD/LBP	Liu et al. [87]	88.92	82.25	88.16	85.76	79.36	90.78
RD/CI/LBP	Liu et al. [87]	89.54	81.45	88.51	81.84	78.79	94.31
NI/CI/LBP	Liu et al. [87]	83.25	72.63	82.13	81.75	76.43	89.09
NI/RD/CI/LBP	Liu et al. [87]	89.07	83.08	88.57	85.26	79.38	93.62
DCP	Ding et al. [88]	87.86	69.54	77.76	70.72	70.83	87.82
DRLBP	Mehta and Egiazarian [89]	91.29	80.00	91.74	71.47	77.55	94.12
ELGS	Bashier et al. [90]	93.12	85.16	89.22	87.12	81.38	92.48
LMEBP	Subrahmanyam et al. [91]	88.92	82.49	87.55	75.43	76.65	94.85
MMEPOP	Vipparthi et al. [92]	82.03	71.72	81.17	73.30	70.76	87.95
SMEPOP	Vipparthi et al. [92]	90.13	79.42	85.17	76.76	77.41	91.16
LBPV	Guo et al. [93]	82.74	77.78	86.74	84.20	76.53	85.19
LBPD	Hong et al. [94]	9.87	8.16	26.76	41.33	19.60	20.73
ALBP	Guo et al. [95]	79.06	60.25	77.24	70.47	69.71	85.64
RDLBP	Liu et al. [87]	89.83	80.37	86.42	82.16	78.25	90.65
NTLBP	Fathi and Naghsh-Nilchi [96]	72.27	55.62	70.73	63.25	69.02	87.39
DCLBP	Ylioinas et al. [97]	88.42	82.66	89.33	89.53	78.13	91.63
3DLBP	Huang et al. [98]	85.99	83.09	89.62	85.45	77.34	91.60
BGC1	Fernández et al. [99]	92.76	82.66	90.83	84.49	79.09	91.64
BGC2	Fernández et al. [99]	91.35	80.04	85.00	77.52	76.72	90.73
BGC3	Fernández et al. [99]	88.59	80.65	85.59	76.37	76.32	90.43
D-LBP	Xiaosheng and Junding [100]	80.62	65.03	85.18	78.00	74.19	85.89
LOSIB	Garca-Olalla et al. [101]	35.77	37.56	70.24	64.26	46.72	52.86
ID-LBP	Xiaosheng and Junding [100]	78.01	59.94	77.36	74.43	69.91	82.03
LBP	Ojala et al. [13]	91.03	81.63	89.63	79.96	77.97	91.59
LPQ	Ojansivu and Heikkila [102]	89.19	79.83	86.94	84.07	77.40	91.99
MBP	Hafiane et al. [103]	88.75	83.51	89.09	85.46	77.54	90.88
LQP	Nanni et al. [104]	89.66	87.86	92.66	89.34	81.51	93.15
dLBPα	Kaya et al. [40]	90.13	56.52	78.68	64.27	72.05	92.20
nLBPd	Kaya et al. [40]	92.76	82.66	90.83	84.49	79.09	91.64

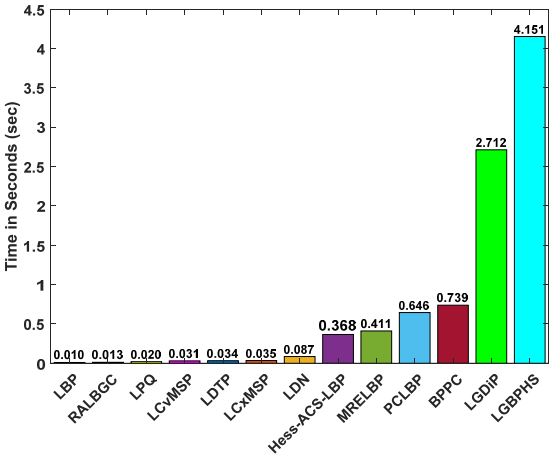

FIGURE 7. The processing time (in seconds) of the 13 LBP descriptors.

BPPC [35], LGDiP [34], LGBPHS [33] methods are used for time comparison. While the developed method increased the classification accuracy of the ACS-LBP method, it has increased the computational cost partially due to the Hessian matrix calculation. Nevertheless, since hessian matrix computation isn't very time-consuming, the proposed Hess-ACS-LBP method might be suitable both in the scenarios of content based image retrieval and real time application.

VII. CONCLUSION

In this study, a LBP based hybrid method with Hessian matrix and ACS-LBP was proposed. The Hessian matrix with different scales expresses the pixel fluctuations in the window detaily. The magnitude of the derivative components of the Hessian matrix in the horizontal and vertical directions was calculated. By integrating magnitude into the ACS-LBP method, more distinctive LBP features of the texture image were obtained. Thus, a powerful LBP histogram was designed to analyze multi-resolution and different neighborhood relations. Unlike traditional LBP methods, geometric pixel analysis of texture image was performed and the LBP feature vector was constructed. Experimental studies have shown that the proposed method gives better results than traditional LBP and deep learning-based methods.

However, it is worth noting that the performance of the proposed Hess-ACS-LBP is a bit sensitive to the radius R and sigma parameter σ. Also, the automatic determination of the radius and sigma parameters has not been fully investigated. In our future work, we are willing to select the optimal radius and sigma parameters automatically. Finally, based on the proposed descriptor, we plan to develop a hybrid method that uses both graph theory and the proposed Hess-ACS-LBP for many applications such as object tracking, semantic segmentation.

REFERENCES

[1] L. Liu, J. Chen, P. Fieguth, G. Zhao, R. Chellappa, and M. Pietikäinen, "From BoW to CNN: Two decades of texture representation for texture classification," *Int. J. Comput. Vis.*, vol. 127, no. 1, pp. 74–109, Jan. 2019.
[2] J. Chaki and N. Dey, *Texture Feature Extraction Techniques for Image Recognition*. Singapore: Springer-Verlag, 2020.
[3] M. Varma and A. Zisserman, "A statistical approach to texture classification from single images," *Int. J. Comput. Vis.*, vol. 62, nos. 1–2, pp. 61–81, Apr. 2005.
[4] P. P. Ohanian and R. C. Dubes, "Performance evaluation for four classes of textural features," *Pattern Recognit.*, vol. 25, no. 8, pp. 819–833, Aug. 1992.
[5] L. Moraru, S. Moldovanu, L. T. Dimitrievici, N. Dey, A. S. Ashour, F. Shi, S. J. Fong, S. Khan, and A. Biswas, "Gaussian mixture model for texture characterization with application to brain DTI images," *J. Adv. Res.*, vol. 16, pp. 15–23, Mar. 2019.
[6] A. Speis and G. Healey, "Feature extraction for texture discrimination via random field models with random spatial interaction," *IEEE Trans. Image Process.*, vol. 5, no. 4, pp. 635–645, Apr. 1996.
[7] R. L. Kashyap and A. Khotanzad, "A model-based method for rotation invariant texture classification," *IEEE Trans. Pattern Anal. Mach. Intell.*, vol. PAMI-8, no. 4, pp. 472–481, Jul. 1986.
[8] W.-K. Lam and C.-K. Li, "Rotated texture classification by improved iterative morphological decomposition," *IEE Proc.-Vis., Image, Signal Process.*, vol. 144, no. 3, p. 171, 1997.
[9] J. Chaki, N. Dey, L. Moraru, and F. Shi, "Fragmented plant leaf recognition: Bag-of-features, fuzzy-color and edge-texture histogram descriptors with multi-layer perceptron," *Optik*, vol. 181, pp. 639–650, Mar. 2019.
[10] T. Randen and J. H. Husoy, "Filtering for texture classification: A comparative study," *IEEE Trans. Pattern Anal. Mach. Intell.*, vol. 21, no. 4, pp. 291–310, Apr. 1999.
[11] R. M. Haralick, K. Shanmugam, and I. Dinstein, "Textural features for image classification," *IEEE Trans. Syst., Man, Cybern.*, vol. SMC-3, no. 6, pp. 610–621, Nov. 1973.
[12] G. R. Cross and A. K. Jain, "Markov random field texture models," *IEEE Trans. Pattern Anal. Mach. Intell.*, vol. PAMI-5, no. 1, pp. 25–39, Jan. 1983.
[13] T. Ojala, M. Pietikäinen, and D. Harwood, "A comparative study of texture measures with classification based on featured distributions," *Pattern Recognit.*, vol. 29, no. 1, pp. 51–59, Jan. 1996.
[14] T. Ojala, M. Pietikainen, and T. Maenpaa, "Multiresolution gray-scale and rotation invariant texture classification with local binary patterns," *IEEE Trans. Pattern Anal. Mach. Intell.*, vol. 24, no. 7, pp. 971–987, Jul. 2002.
[15] Y. Wang, F. Shi, L. Cao, N. Dey, Q. Wu, A. S. Ashour, R. S. Sherratt, V. Rajinikanth, and L. Wu, "Morphological segmentation analysis and texture-based support vector machines classification on mice liver fibrosis microscopic images," *Current Bioinf.*, vol. 14, no. 4, pp. 282–294, Apr. 2019.
[16] P. Subudhi and S. Mukhopadhyay, "An efficient graph reduction framework for interactive texture segmentation," *Signal Process., Image Commun.*, vol. 74, pp. 42–53, May 2019.
[17] C. Li, Y. Huang, and L. Zhu, "Color texture image retrieval based on Gaussian copula models of Gabor wavelets," *Pattern Recognit.*, vol. 64, pp. 118–129, Apr. 2017.
[18] T. Fang, R. Su, L. Xie, Q. Gu, Q. Li, P. Liang, and T. Wang, "Retinal vessel landmark detection using deep learning and hessian matrix," in *Proc. 8th Int. Congr. Image Signal Process. (CISP)*, Oct. 2015, pp. 387–392.
[19] Y. Song, S. Zhang, B. He, Q. Sha, Y. Shen, T. Yan, R. Nian, and A. Lendasse, "Gaussian derivative models and ensemble extreme learning machine for texture image classification," *Neurocomputing*, vol. 277, pp. 53–64, Feb. 2018.
[20] K. Hanbay, N. Alpaslan, M. F. Talu, D. Hanbay, A. Karci, and A. F. Kocamaz, "Continuous rotation invariant features for gradient-based texture classification," *Comput. Vis. Image Understand.*, vol. 132, pp. 87–101, Mar. 2015.
[21] N. Dalal and B. Triggs, "Histograms of oriented gradients for human detection," in *Proc. IEEE Comput. Soc. Conf. Comput. Vis. Pattern Recognit. (CVPR)*, vol. 1, Jun. 2005, pp. 886–893.
[22] A. R. Rivera, J. R. Castillo, and O. O. Chae, "Local directional number pattern for face analysis: Face and expression recognition," *IEEE Trans. Image Process.*, vol. 22, no. 5, pp. 1740–1752, May 2013.
[23] X. Bu, Y. Wu, Z. Gao, and Y. Jia, "Deep convolutional network with locality and sparsity constraints for texture classification," *Pattern Recognit.*, vol. 91, pp. 34–46, Jul. 2019.
[24] X. Qi, C.-G. Li, G. Zhao, X. Hong, and M. Pietikäinen, "Dynamic texture and scene classification by transferring deep image features," *Neurocomputing*, vol. 171, pp. 1230–1241, Jan. 2016.

[25] J. Zhang, Y. Xie, Q. Wu, and Y. Xia, "Medical image classification using synergic deep learning," *Med. Image Anal.*, vol. 54, pp. 10–19, May 2019.
[26] M. Talo, U. B. Baloglu, Ö. Yıldırım, and U. R. Acharya, "Application of deep transfer learning for automated brain abnormality classification using MR images," *Cognit. Syst. Res.*, vol. 54, pp. 176–188, May 2019.
[27] S. Ren, K. He, R. Girshick, and J. Sun, "Faster R-CNN: Towards real-time object detection with region proposal networks," in *Proc. Adv. Neural Inf. Process. Syst. (NIPS)*, 2015, pp. 91–99.
[28] C. Zhao *et al.*, "A deep learning based anti-aliasing self super-resolution algorithm for MRI," in *Proc. Int. Conf. Med. Image Comput. Comput.-Assist. Intervent.*, Cham, Switzerland: Springer, 2018, pp. 100–108.
[29] I. El Khadiri, A. Chahi, Y. El Merabet, Y. Ruichek, and R. Touahni, "Local directional ternary pattern: A new texture descriptor for texture classification," *Comput. Vis. Image Understand.*, vol. 169, pp. 14–27, Apr. 2018.
[30] L. Liu, S. Lao, P. W. Fieguth, Y. Guo, X. Wang, and M. Pietikäinen, "Median robust extended local binary pattern for texture classification," *IEEE Trans. Image Process.*, vol. 25, no. 3, pp. 1368–1381, Mar. 2016.
[31] Z. Pan, Z. Li, H. Fan, and X. Wu, "Feature based local binary pattern for rotation invariant texture classification," *Expert Syst. Appl.*, vol. 88, pp. 238–248, Dec. 2017.
[32] F. Yuan, X. Xia, and J. Shi, "Mixed co-occurrence of local binary patterns and Hamming-distance-based local binary patterns," *Inf. Sci.*, vols. 460–461, pp. 202–222, Sep. 2018.
[33] W. Zhang, S. Shan, W. Gao, X. Chen, and H. Zhang, "Local Gabor binary pattern histogram sequence (LGBPHS): A novel non-statistical model for face representation and recognition," in *Proc. 10th IEEE Int. Conf. Comput. Vis. (ICCV)*, vol. 1, 2005, pp. 786–791.
[34] S. M. Z. Ishraque, A. K. M. H. Banna, and O. Chae, "Local Gabor directional pattern for facial expression recognition," in *Proc. 15th Int. Conf. Comput. Inf. Technol. (ICCIT)*, Dec. 2012, pp. 164–167.
[35] S. Shojaeilangari, W.-Y. Yau, J. Li, and E.-K. Teoh, "Feature extraction through binary pattern of phase congruency for facial expression recognition," in *Proc. 12th Int. Conf. Control Autom. Robot. Vis. (ICARCV)*, Dec. 2012, pp. 166–170.
[36] S. Naeem, F. Riaz, A. Hassan, and R. Nisar, "Description of visual content in dermoscopy images using joint histogram of multiresolution local binary patterns and local contrast," in *Proc. Int. Conf. Intell. Data Eng. Automated Learn.*, 2015, pp. 433–440.
[37] M. Heikkilä, M. Pietikäinen, and C. Schmid, "Description of interest regions with center-symmetric local binary patterns," in *Computer Vision, Graphics and Image Processing*. Berlin, Germany: Springer, 2006, pp. 58–69.
[38] S. Liao, M. W. K. Law, and A. C. S. Chung, "Dominant local binary patterns for texture classification," *IEEE Trans. Image Process.*, vol. 18, no. 5, pp. 1107–1118, May 2009.
[39] F. Liu, Z. Tang, and J. Tang, "WLBP: Weber local binary pattern for local image description," *Neurocomputing*, vol. 120, pp. 325–335, Nov. 2013.
[40] Y. Kaya, Ö. F. Ertuğrul, and R. Tekin, "Two novel local binary pattern descriptors for texture analysis," *Appl. Soft Comput.*, vol. 34, pp. 728–735, Sep. 2015.
[41] C. Singh, E. Walia, and K. P. Kaur, "Color texture description with novel local binary patterns for effective image retrieval," *Pattern Recognit.*, vol. 76, pp. 50–68, Apr. 2018.
[42] S. H. Lee, J. Y. Choi, Y. M. Ro, and K. N. Plataniotis, "Local color vector binary patterns from multichannel face images for face recognition," *IEEE Trans. Image Process.*, vol. 21, no. 4, pp. 2347–2353, Apr. 2012.
[43] Y. El Merabet and Y. Ruichek, "Local concave-and-convex micro-structure patterns for texture classification," *Pattern Recognit.*, vol. 76, pp. 303–322, Apr. 2018.
[44] I. El Khadiri, M. Kas, Y. El Merabet, Y. Ruichek, and R. Touahni, "Repulsive-and-attractive local binary gradient contours: New and efficient feature descriptors for texture classification," *Inf. Sci.*, vol. 467, pp. 634–653, Oct. 2018.
[45] Q. Kou, D. Cheng, L. Chen, and Y. Zhuang, "Principal curvatures based local binary pattern for rotation invariant texture classification," *Optik*, vol. 193, Sep. 2019, Art. no. 162999.
[46] Z. Guo, Q. Li, L. Zhang, J. You, D. Zhang, and W. Liu, "Is local dominant orientation necessary for the classification of rotation invariant texture?" *Neurocomputing*, vol. 116, pp. 182–191, Sep. 2013.
[47] Q. Kou, D. Cheng, H. Zhuang, and R. Gao, "Cross-complementary local binary pattern for robust texture classification," *IEEE Signal Process. Lett.*, vol. 26, no. 1, pp. 129–133, Jan. 2019.
[48] K. Hanbay, N. Alpaslan, M. F. Talu, and D. Hanbay, "Principal curvatures based rotation invariant algorithms for efficient texture classification," *Neurocomputing*, vol. 199, pp. 77–89, Jul. 2016.
[49] M. Altın, A. Kazan, and H. B. Karadağ, "Rotational surfaces generated by planar curves in E^3 with density," *Int. J. Anal. Appl.*, vol. 17, no. 3, pp. 311–328, 2019.
[50] M. Altın, A. Kazan, and H. B. Karadağ, "Ruled surfaces in E^3 with density," *Honam Math. J.*, vol. 41, no. 4, pp. 683–695, 2019.
[51] Y. El Merabet, Y. Ruichek, and A. El Idrissi, "Attractive-and-repulsive center-symmetric local binary patterns for texture classification," *Eng. Appl. Artif. Intell.*, vol. 78, pp. 158–172, Feb. 2019.
[52] Y. Tang, L. Jiang, Y. Hou, and R. Wang, "Contactless fingerprint image enhancement algorithm based on hessian matrix and STFT," in *Proc. 2nd Int. Conf. Multimedia Image Process. (ICMIP)*, Mar. 2017, pp. 156–160.
[53] S. Godbole and S. Sarawagi, "Discriminative methods for multi-labeled classification," in *Proc. Pacific–Asia Conf. Knowl. Discovery Data Mining*. Berlin, Germany: Springer, 2004, pp. 22–30.
[54] K. J. Dana, B. van Ginneken, S. K. Nayar, and J. J. Koenderink, "Reflectance and texture of real-world surfaces," *ACM Trans. Graph.*, vol. 18, no. 1, pp. 1–34, Jan. 1999.
[55] A. R. Backes, D. Casanova, and O. M. Bruno, "Color texture analysis based on fractal descriptors," *Pattern Recognit.*, vol. 45, no. 5, pp. 1984–1992, May 2012.
[56] B. Caputo, E. Hayman, and P. Mallikarjuna, "Class-specific material categorisation," in *Proc. 10th IEEE Int. Conf. Comput. Vis. (ICCV)*, vol. 2, Oct. 2005, pp. 1597–1604.
[57] A. Fernández, M. X. Álvarez, and F. Bianconi, "Texture description through histograms of equivalent patterns," *J. Math. Imag. Vis.*, vol. 45, no. 1, pp. 76–102, Jan. 2013.
[58] T. Ojala, T. Mäenpää, M. Pietikäinen, J. Viertola, J. Kyllönen, and S. Huovinen, "Outex—New framework for empirical evaluation of texture analysis algorithms," in *Proc.-Int. Conf. Pattern Recognit.*, 2002, vol. 16, no. 1, pp. 701–706.
[59] Y. Xu, H. Ji, and C. Fermüller, "Viewpoint invariant texture description using fractal analysis," *Int. J. Comput. Vis.*, vol. 83, no. 1, pp. 85–100, Jun. 2009.
[60] G. J. Burghouts and J.-M. Geusebroek, "Material-specific adaptation of color invariant features," *Pattern Recognit. Lett.*, vol. 30, no. 3, pp. 306–313, Feb. 2009.
[61] *Department of Computer Sciences, U.S., Salzburg Texture Image Database (STex)*. Accessed: Dec. 26, 2019. [Online]. Available: http://wavelab.at/sources/STex/
[62] *VisTex, Texture Dataset*. Accessed: Dec. 26, 2019. [Online]. Available: https://vismod.media.mit.edu/vismod/imagery/VisionTexture/vistex.html
[63] P. Brodatz, *Textures: A Photographic Album for Artists and Designers*. New York, NY, USA: Dover, 1966.
[64] Z. Guo, L. Zhang, and D. Zhang, "A completed modeling of local binary pattern operator for texture classification," *IEEE Trans. Image Process.*, vol. 19, no. 6, pp. 1657–1663, Jun. 2010.
[65] P. Liu, J.-M. Guo, C.-Y. Wu, and D. Cai, "Fusion of deep learning and compressed domain features for content-based image retrieval," *IEEE Trans. Image Process.*, vol. 26, no. 12, pp. 5706–5717, Dec. 2017.
[66] S. K. Choy and C. S. Tong, "Statistical wavelet subband characterization based on generalized gamma density and its application in texture retrieval," *IEEE Trans. Image Process.*, vol. 19, no. 2, pp. 281–289, Feb. 2010.
[67] R. Kwitt, P. Meerwald, and A. Uhl, "Efficient texture image retrieval using copulas in a Bayesian framework," *IEEE Trans. Image Process.*, vol. 20, no. 7, pp. 2063–2077, Jul. 2011.
[68] G. Verdoolaege, S. De Backer, and P. Scheunders, "Multiscale colour texture retrieval using the geodesic distance between multivariate generalized Gaussian models," in *Proc. 15th IEEE Int. Conf. Image Process. (ICIP)*, Oct. 2008, pp. 169–172.
[69] J.-M. Guo and H. Prasetyo, "Content-based image retrieval using features extracted from halftoning-based block truncation coding," *IEEE Trans. Image Process.*, vol. 24, no. 3, pp. 1010–1024, Mar. 2015.
[70] J.-M. Guo, H. Prasetyo, and N.-J. Wang, "Effective image retrieval system using dot-diffused block truncation coding features," *IEEE Trans. Multimedia*, vol. 17, no. 9, pp. 1576–1590, Sep. 2015.
[71] M. Verma, B. Raman, and S. Murala, "Local extrema co-occurrence pattern for color and texture image retrieval," *Neurocomputing*, vol. 165, pp. 255–269, Oct. 2015.

[72] M.-T. Pham, G. Mercier, and L. Bombrun, "Color texture image retrieval based on local extrema features and Riemannian distance," *J. Imag.*, vol. 3, no. 4, p. 43, Oct. 2017.
[73] A. Krizhevsky, I. Sutskever, and G. E. Hinton, "ImageNet classification with deep convolutional neural networks," in *Proc. Int. Conf. Neural Inf. Process. Syst.*, 2012, pp. 1097–1105.
[74] K. Simonyan and A. Zisserman, "Very deep convolutional networks for large-scale image recognition," in *Proc. 3rd Int. Conf. Learn. Represent. (ICLR)*, 2015, pp. 1–14.
[75] C. Szegedy, W. Liu, Y. Jia, P. Sermanet, S. Reed, D. Anguelov, D. Erhan, V. Vanhoucke, and A. Rabinovich, "Going deeper with convolutions," in *Proc. IEEE Conf. Comput. Vis. Pattern Recognit. (CVPR)*, Jun. 2015, pp. 1–9.
[76] K. He, X. Zhang, S. Ren, and J. Sun, "Deep residual learning for image recognition," in *Proc. IEEE Conf. Comput. Vis. Pattern Recognit. (CVPR)*, Jun. 2016, pp. 770–778.
[77] C. Li, Y. Huang, X. Yang, and H. Chen, "Marginal distribution covariance model in the multiple wavelet domain for texture representation," *Pattern Recognit.*, vol. 92, pp. 246–257, Aug. 2019.
[78] M. R. Faraji and X. Qi, "Face recognition under varying illuminations using logarithmic fractal dimension-based complete eight local directional patterns," *Neurocomputing*, vol. 199, pp. 16–30, Jul. 2016.
[79] S. Dong, J. Yang, C. Wang, Y. Chen, and D. Sun, "A new finger vein recognition method based on the difference symmetric local graph structure (DSLGS)," *Int. J. Signal Process., Image Process. Pattern Recognit.*, vol. 8, no. 10, pp. 71–80, Oct. 2015.
[80] A. R. Rivera, J. R. Castillo, and O. Chae, "Local directional texture pattern image descriptor," *Pattern Recognit. Lett.*, vol. 51, pp. 94–100, Jan. 2015.
[81] Z. Zhu, X. You, C. L. P. Chen, D. Tao, W. Ou, X. Jiang, and J. Zou, "An adaptive hybrid pattern for noise-robust texture analysis," *Pattern Recognit.*, vol. 48, no. 8, pp. 2592–2608, Aug. 2015.
[82] Y. Xu, S. Huang, H. Ji, and C. Fermüller, "Scale-space texture description on SIFT-like textons," *Comput. Vis. Image Understand.*, vol. 116, no. 9, pp. 999–1013, Sep. 2012.
[83] M. Verma and B. Raman, "Local neighborhood difference pattern: A new feature descriptor for natural and texture image retrieval," *Multimedia Tools Appl.*, vol. 77, no. 10, pp. 11843–11866, May 2018.
[84] S. Chakraborty, S. K. Singh, and P. Chakraborty, "Local quadruple pattern: A novel descriptor for facial image recognition and retrieval," *Comput. Electr. Eng.*, vol. 62, pp. 92–104, Aug. 2017.
[85] A. Pillai, R. Soundrapandiyan, S. Satapathy, S. C. Satapathy, K.-H. Jung, and R. Krishnan, "Local diagonal extrema number pattern: A new feature descriptor for face recognition," *Future Gener. Comput. Syst.*, vol. 81, pp. 297–306, Apr. 2018.
[86] S. R. Dubey, S. K. Singh, and R. K. Singh, "Multichannel decoded local binary patterns for content-based image retrieval," *IEEE Trans. Image Process.*, vol. 25, no. 9, pp. 4018–4032, Sep. 2016.
[87] L. Liu, L. Zhao, Y. Long, G. Kuang, and P. Fieguth, "Extended local binary patterns for texture classification," *Image Vis. Comput.*, vol. 30, no. 2, pp. 86–99, Feb. 2012.
[88] C. Ding, J. Choi, D. Tao, and L. S. Davis, "Multi-directional multi-level dual-cross patterns for robust face recognition," *IEEE Trans. Pattern Anal. Mach. Intell.*, vol. 38, no. 3, pp. 518–531, Mar. 2016.
[89] R. Mehta and K. Egiazarian, "Dominant rotated local binary patterns (DRLBP) for texture classification," *Pattern Recognit. Lett.*, vol. 71, pp. 16–22, Feb. 2016.
[90] H. K. Bashier, L. S. Hoe, L. T. Hui, M. F. Azli, P. Y. Han, W. K. Kwee, and M. S. Sayeed, "Texture classification via extended local graph structure," *Optik*, vol. 127, no. 2, pp. 638–643, Jan. 2016.
[91] M. Subrahmanyam, R. P. Maheshwari, and R. Balasubramanian, "Local maximum edge binary patterns: A new descriptor for image retrieval and object tracking," *Signal Process.*, vol. 92, no. 6, pp. 1467–1479, Jun. 2012.
[92] S. K. Vipparthi, S. Murala, S. K. Nagar, and A. B. Gonde, "Local Gabor maximum edge position octal patterns for image retrieval," *Neurocomputing*, vol. 167, pp. 336–345, Nov. 2015.
[93] Z. Guo, L. Zhang, and D. Zhang, "Rotation invariant texture classification using LBP variance (LBPV) with global matching," *Pattern Recognit.*, vol. 43, no. 3, pp. 706–719, Mar. 2010.
[94] X. Hong, G. Zhao, M. Pietikainen, and X. Chen, "Combining LBP difference and feature correlation for texture description," *IEEE Trans. Image Process.*, vol. 23, no. 6, pp. 2557–2568, Jun. 2014.
[95] Z. Guo, L. Zhang, D. Zhang, and S. Zhang, "Rotation invariant texture classification using adaptive LBP with directional statistical features," in *Proc. IEEE Int. Conf. Image Process.*, Sep. 2010, pp. 285–288.
[96] A. Fathi and A. R. Naghsh-Nilchi, "Noise tolerant local binary pattern operator for efficient texture analysis," *Pattern Recognit. Lett.*, vol. 33, no. 9, pp. 1093–1100, Jul. 2012.
[97] J. Ylioinas, A. Hadid, Y. Guo, and M. Pietikäinen, "Efficient image appearance description using dense sampling based local binary patterns," in *Proc. Asian Conf. Comput. Vis.*. Berlin, Germany: Springer, 2012, pp. 375–388.
[98] Y. Huang, Y. Wang, and T. Tan, "Combining statistics of geometrical and correlative features for 3D face recognition," in *Proc. Brit. Mach. Vis. Conf.*, 2006, pp. 879–888.
[99] A. Fernández, M. X. Álvarez, and F. Bianconi, "Image classification with binary gradient contours," *Opt. Lasers Eng.*, vol. 49, nos. 9–10, pp. 1177–1184, Sep. 2011.
[100] X. Wu and J. Sun, "An effective texture spectrum descriptor," in *Proc. 5th Int. Conf. Inf. Assurance Secur. (IAS)*, vol. 2, 2009, pp. 361–364.
[101] O. Garcia-Olalla, E. Alegre, L. Fernández-Robles, and V. González-Castro, "Local oriented statistics information booster (LOSIB) for texture classification," in *Proc. 22nd Int. Conf. Pattern Recognit.*, Aug. 2014, pp. 1114–1119.
[102] V. Ojansivu and J. Heikkilä, "Blur insensitive texture classification using local phase quantization," in *Image and Signal Processing* (Lecture Notes in Computer Science: Lecture Notes in Artificial Intelligence: Lecture Notes in Bioinformatics), vol. 5099, 2008, pp. 236–243.
[103] A. Hafiane, G. Seetharaman, and B. Zavidovique, "Median binary pattern for textures classification," in *Proc. 4th Int. Conf. Image Anal. Recognit. (ICIAR)*, vol. 4633, 2007, pp. 387–398.
[104] L. Nanni, A. Lumini, and S. Brahnam, "Local binary patterns variants as texture descriptors for medical image analysis," *Artif. Intell. Med.*, vol. 49, no. 2, pp. 117–125, Jun. 2010.

NUH ALPASLAN received the B.D.S. degree in computer engineering from Fırat University, Elazig, Turkey, in 2010, and the Ph.D. degree in computer engineering from İnönü University, in 2017. His current research interests include computer vision and image processing.

KAZIM HANBAY was born in Malatya, Turkey, in 1983. He received the B.D.S. degree in computer science from Kocaeli University, Kocaeli, Turkey, in 2004, and the Ph.D. degree in computer engineering from İnönü University, in 2016. His current research interests include machine learning, pattern recognition, and image processing.